Check for updates

Elastic/viscoelastic polymer bilayers: a model-based approach to stretch-responsive constructs†

Austin S. Mills, [iD] ‡*[a] Evan Chou, [iD] ‡[b] Zachary Baierl, [iD] [b] Kathryn A. Daltorio*[a] and Gary E. Wnek*[b]

The use of polymers in the fabrication of bilayers for stimuli-responsive systems is well-known, yet viscoelasticity and viscoelastic models representing bilayer behavior have received surprisingly little attention. Of particular recent interest to us are simple polymeric bilayers in which one material, such as styrene–ethylene–propylene–styrene (SEPS) or styrene–isobutylene–styrene (SIBS), shows typical rubbery elastic response upon extension and retraction, and the other, an unvulcanized, low-T_g polymer such as butyl rubber (butyl), exhibits a viscoelastic response. When such a bilayer strip is extended to a fixed strain and held for several seconds followed by sudden release of this strain, rapid curling is observed, achieving a maximum curvature within 1 second, with a gradual uncurling, typically taking 300–600 seconds to eventually return to a flat strip. Attention has been directed to modeling the observed bilayer behavior. We compare predicted curvature and relaxation time constants from finite element analysis (FEA) simulations using Maxwell, Zener, Generalized Maxwell, and Parallel Rheological Framework (PRF) viscoelastic models to the experimentally measured values. We find that the Generalized Maxwell model predicts curvature over time with the lowest overall mean absolute scaled error (MASE) of 0.519, corresponding to a 4.9% difference from the second lowest error model and a 76.8% difference from the highest error model. Building upon an understanding of the material mechanics in simple bilayer strips, more complex bilayer systems can be designed. Samples of cross and weave geometries were fabricated from bilayer films and initial testing demonstrates how these materials can be used in potential applications.

1 Introduction

Soft polymer materials intrinsically provide many degrees of freedom and the potential to adapt to complex environments. Their response to external stimuli, such as heat, light, electricity, and moisture are well-studied, although in practice, many of these are still difficult to precisely control and their variability complicates their use.[1–3] One common feature in all of them is viscoelasticity, which is often relegated to a passive component contribution, serving either as a platform for the stimuli-responsive element[4,5] or chemically modified to provide a flexible polymer backbone to the system.[6] However, viscoelasticity in itself can be considered stimuli-responsive, so treating it as an ignored passive element can lead to

unforeseen complications. Furthermore, modern devices often require more than a single material or composite and utilize intelligent structural design,[7–9] which makes it even more difficult to predict how these systems of materials will behave. One way to impart intelligence to viscoelastic materials is by fabricating a bilayer, in which a time-dependent strain mismatch resulting from how the two materials respond to external stimuli generates a characteristic bending motion.[10–12] Bilayer systems can include organic[13] or inorganic materials,[14] and curvature can be driven by stimuli such as heat,[15–17] light,[18–20] and moisture,[21–23] or any other variable that can induce deformation in a material. A tough hydrogel system has recently been reported for use in soft robotics with an initial evaluation of viscoelastic bilayer mismatch before ultimately focusing on single layer controlled shape change *via* localized chemical masking and magnetic elements.[24] Much less explored is the viscoelastic material response and corresponding modeling of thermoplastic bilayers driven by tension and release of strain. Of primary interest to this work are a predominantly elastic layer such as a styrenic thermoplastic elastomer (*e.g.* styrene-*b*-ethylene-*b*-propylene-*b*-styrene),[25] SEPS and a predominantly viscous layer such as unvulcanized poly(isobutylene), known as butyl rubber, butyl.[26,27] Butyl demonstrates strain rate

[a] *Department of Mechanical and Aerospace Engineering, Case Western Reserve University, Cleveland, Ohio, USA. E-mail: austin.mills@case.edu, kathryn.daltorio@case.edu*

[b] *Department of Macromolecular Science and Engineering, Case Western Reserve University, Cleveland, Ohio, USA. E-mail: gary.wnek@case.edu*

† Electronic supplementary information (ESI) available. See DOI: https://doi.org/10.1039/d3sm01004j

‡ Austin S. Mills and Evan Chou contributed equally to this work and share first authorship.

dependent viscoelastic behavior, a property which can be exploited to develop new soft metamaterials, loosely defined as materials which act contrary to what we expect from nature.[28] Unlike the materials described in the aforementioned hydrogel system,[24] as well as a recently reported ion gel bilayer system,[29] thermoplastic bilayer systems rely primarily on molecular entanglements between the two layers and an intrinsic mismatch of viscoelastic properties, without involving complications due to hydrogen bonding, inter-chain covalent bonding, and solvent-dependent phenomena found in gel systems. Understanding how viscoelasticity can be exploited to achieve complex motion may lead to improvements in the performance of stimuli-responsive materials and systems.

Many polymer systems can be adequately described by simple viscoelastic Maxwell or Zener models,[30] but more complex models such as the Generalized Maxwell and the parallel rheological framework can in theory provide a more accurate recreation of physical phenomena like relaxation and viscous flow.[31,32] These viscoelastic models can be implemented into finite element simulations and their results can be compared with experimental stress and relaxation data to determine how closely the viscoelastic models predict the behavior of bilayers strips as well as more complex bilayer architectures. Currently, there is no universal standard for testing the curvature of a viscoelastic bilayer. Varying strain-hold-release experiments are necessary for curvature analysis because the butyl component behaves differently based on the path-dependent loading and unloading conditions.[33] Materials like butyl can alternate between elastic recovery and creep based on these conditions. Of particular interest is a point known as the relaxation time constant, which describes the overall viscoelastic relaxation behavior of a bilayer and other designs.[34] Knowledge of relaxation time constants is useful when modeling and controlling the behavior of compliant intelligent structures, so they can be designed to adapt as desired to changes in the environment.

This modeling-and-experimental approach is first applied to a simple bilayer strip system, but more complex architectures and motions can be achieved through alternative fabrication techniques. For example, melt pressing films of two polymeric materials and then laminating them together is an effective strategy for producing bilayers, but is more restrictive when aiming to design more complex patterns, like grippers for soft robotics. In addition, layer adhesion may be improved by a variety of methods such as by selecting materials with greater compatibility. This can open up the possibility for 3D printing which leads to improvements in pattern resolution compared to melt pressing of films and is widely used for prototyping soft devices.[35]

2 Experimental

2.1 Materials and melt-press fabrication of films, bilayer and trilayer sheets

Two Carver Inc. Model 4122 presses were used in the melt-press fabrication of the films and bilayer sheets within this work: the first to heat and the second to quench. Layers of Teflon®-coated aluminum sheets were used on both sides of the sample to facilitate removal of the film after pressing. The foil was then bounded by thin aluminum sheets for pressure transfer and handling of the assembly. Film thicknesses were controlled via the use of different thickness sheet metal that was cut into a hollow frame insert surrounding the film. All created films aside from the adhesion samples were formed under a load of 10 000 lbs. All individual layers were formed using a multistage cycle to allow for air removal. Depending on the film thickness, a 5–10 minute preheat was followed by a 5–10 minute hold. This was followed by two more cycles of alternating heat and hold at about 5 minutes each. Finally, the films were quenched for several minutes using the second Carver Inc. press with water cooled platens and hand set pressure. After inspection some individual films underwent an additional cycle or two depending on the quality.

Films of SEPS (SEPTON™ 2002 and SEPTON™ 2004 from Kuraray Co., Ltd) and SIBS (SIBSTAR™ 073T from Kaneka Co.) were prepared individually by pressing the raw material pellets in a 17.8 cm × 27.9 cm × 0.18 mm die using the multistage cycle described above at 120–165 °C and 165 °C respectively. Dies used within this work refer to rectangular sheets with an inlaid cavity in which material can flow and be pressed into a desired shape and thickness. The resulting films (corresponding to a minimum pressure of 0.89 MPa) of both the SEPS and SIBS had slight, but noticeable variations in thickness. Thicker sheets, for tensile and adhesion testing, of 1.85 ± 0.1 mm were prepared using the same process and a 12.7 cm × 12.7 cm × 2 mm die, corresponding to a minimum pressure of 2.8 MPa.

Films of raw, unvulcanized butyl (butyl 268 from ExxonMobil Co., which contains 98.3 ± 0.2 mol% isobutylene repeat units) were prepared individually from 25 mm thickness slabs. Scissors were used to cut roughly 6 mm thick smaller pieces which were formed into a sheet using a 17.8 cm × 27.9 cm × 0.5 mm die and the multistage process above at 120 °C. The resulting films (corresponding to a minimum pressure of 0.89 MPa) varied in thickness. Thinner sheets using the same process (and pressure) and the 17.8 cm × 27.9 cm × 0.18 mm die were made for the adhesion testing, while thicker sheets using a 17.8 cm × 17.8 cm × 2.8 mm die (corresponding to a minimum pressure of 1.4 MPa) were made for tensile testing.

Production of the bilayer sheets utilized one of each of the premade SEPS and butyl films. The two films were stacked upon each other and set within a 17.8 cm × 27.9 cm × 0.7 mm die. Only the first step of the multistage cycle was used: a 5–10 min preheat at 120 °C then 5–10 °C hold at 10 000 lbf (corresponding to a minimum pressure of 0.89 MPa). The resulting bilayers varied in thickness ranging from 1.80–2.30 mm.

Fabrication of the trilayer samples for adhesion testing consisted of cutting and sandwiching the thin 0.2 mm butyl between two layers of the 1.8 mm SEPS and SIBS. About 25 mm along one side was left free of butyl and was filled with an additional piece of Teflon® coated aluminum sheet. This was to allow for tabs and a clean opening to the adhesive layer. The resulting stack measuring about 6.4 cm × 12.7 cm was then

placed within a 2.8 mm die and allowed to preheat for 5 minutes. The assembly was then pressed at 1000 lbf (corresponding to a starting pressure of 8.6 kPa) for only a couple minutes to avoid forcing the butyl out of the sides. This resulted in samples of thickness 3.5 ± 0.2 mm.

2.2 SEPS testing

SEPS behaves like an elastomer and should generally have springlike properties that can be classified into either elastic or hyperelastic responses (Fig. S2, ESI†). To determine which of these responses is more appropriate for SEPS, a stress–strain curve of the material was obtained. Tensile testing was performed at room temperature on three SEPS (SEPTON™ 2002 and SEPTON™ 2004 from Kuraray Co., Ltd) dog bone specimens cut from a sheet of 1.8 mm ± 0.05 mm thickness according to ASTM D1708. Within this work all mentions of extension rate refer to the crosshead speed on the Instron tensile tester. An Instron 5965 tensile tester (Instron Calibration Laboratory, MA, USA) equipped with a Cat. No. 2580-1KN load cell was used to conduct the testing at an extension rate of 0.50 mm s^{-1} (engineering strain rate, $\dot{\varepsilon}$ = 0.023 1 s^{-1}) (Fig. S2, ESI†) until the sample failed typically near the grips. From these data sets, the SEPS appears to exhibit a linear elastic response until about 50% engineering strain after which a hyperelastic characterization appears more representative of the response as a whole.

2.3 Butyl testing

Cyclic uniaxial tension experiments were performed on raw unvulcanized butyl to measure the viscoelastic response. All butyl testing was performed at room temperature using an ASTM D638 type V dog bone specimen that was cut from the butyl film and tested using an Instron 5965 tensile tester (Instron Calibration Laboratory, MA, USA) equipped with a Cat. No. 2580-1KN load cell. During the cyclic testing the butyl specimens were subjected to cyclic uniaxial tensile holds and releases at increasing butyl engineering strains. Using a constant $\dot{\varepsilon}$, specimens were tensioned to 5% strain, held for 10 seconds, then lowered at a constant engineering strain rate to 0% strain. This process was then repeated sequentially for 10%, 25%, 50%, and 100% engineering strain holds. Three experiments for each of three constant extension rates of 0.1 mm s^{-1}, 0.5 mm s^{-1}, and 1 mm s^{-1}, corresponding to $\dot{\varepsilon}$ of 0.004 1 s^{-1}, 0.02 1 s^{-1} and 0.04 1 s^{-1} respectively, were conducted (Fig. S3, ESI†). The resulting stresses show repeatability (Fig. S4, ESI†).

A stress-softening Mullins effect[36] for butyl was investigated using a cyclic unixial tension experiment during which the butyl was repeatedly tensioned to 30%, held for 10 s, then lowered to 0% engineering strain (Fig. S5a, ESI†). After 5 cycles the maximum stress recorded at the beginning of the holding period had reduced from an initial ~61 kPa to ~30 kPa (Fig. S5b, ESI†).

2.4 Bilayer strip strain-hold-release curvatures

Curvature testing experiments were conducted for the purpose of demonstrating how the bilayer strip curvature responds to varying applications of tension as well as serving as a means of evaluating the predictive quality of the bilayer material models. Bilayer rectangular strips of ~63.5 mm length and ~12.7 mm width were die cut from the prepared bilayer sheet. The strips' total thickness was measured with calipers and ranged from 1.80–2.30 mm. The relative thickness of the SEPS and butyl layers to the total thickness was determined visually. The relative thickness of the SEPS layers ranged from 60–80%, conversely, the butyl layers' relative thickness ranged from 40–20%. Relative thicknesses typically varied along the length of a single sample, which was accounted for in material modeling and analysis. The total thickness and relative thicknesses of each strip can be found in the ESI† (Table S2).

The bilayer strips were mounted vertically at room temperature within the Instron 5965 tensile tester (Instron Calibration Laboratory, MA, USA) equipped with a Cat. No. 2580-1KN load cell with the bilayer's side profile facing outwards for video curvature analysis. The strips were held under slight tension to eliminate slack before being stretched at a constant rate to a set extension, held in place, and then "released" via cutting of the bottom portion of the bilayer near the grips (Fig. 1). An average gauge length of 3.39 cm was used. The hold step was timed with a stopwatch and the bilayer was then cut by hand with scissors.

The extensions, extension rates, and hold times were each varied to demonstrate how each of the parameters affects the curvature response (Table 1). Parameters variations were chosen such that the maximum curvatures achieved didn't result in a collision of the curling bilayer with the Instron grip surfaces.

The bilayers' decaying curvature responses were video recorded with an iPhone 13 camera (1080 p at 30 fps) for at least 10 minutes for the purpose of extracting curvature over time data. The camera was aligned with the post extension position of the bilayer interface with the top clamp to reduce the effect of video perspective distortion on the bilayer. Due to the nature of using hands for scissor cutting the bilayer strips, the camera view is blocked by the hands prior to and shortly after cutting. The time required to remove the hands blocking the camera after cutting and for the camera to automatically refocus on the strip took an average of 1.39 seconds with extremes ranging from 0.4–3.2 seconds. Following recording, the videos files were processed first into a 5 fps form using VLC media player version 3.0.18 from VideoLan for easier handling.

A custom MATLAB (MathWorks) script was written to read the 5 fps video files and analyze the curvatures of the bilayer over time. The video frames corresponding to the moment of the bilayer cutting as well as the moment when the camera reacquired focus on the strip were determined visually and used as input for the script. The script first displays the first frame of the video, prior to any extension, and a position on an inner corner of the top clamp is selected via mouse click; followed by displaying of the last frame of the video where the same corner point, but moved due to strip extension, is again selected via mouse click (Fig. 2a first and second panels). By using knowledge of the extension amount corresponding to the video analyzed, a distance relationship between video pixels and extension is established (Fig. 2a third panel). Next, the previously input frame during which the camera has just
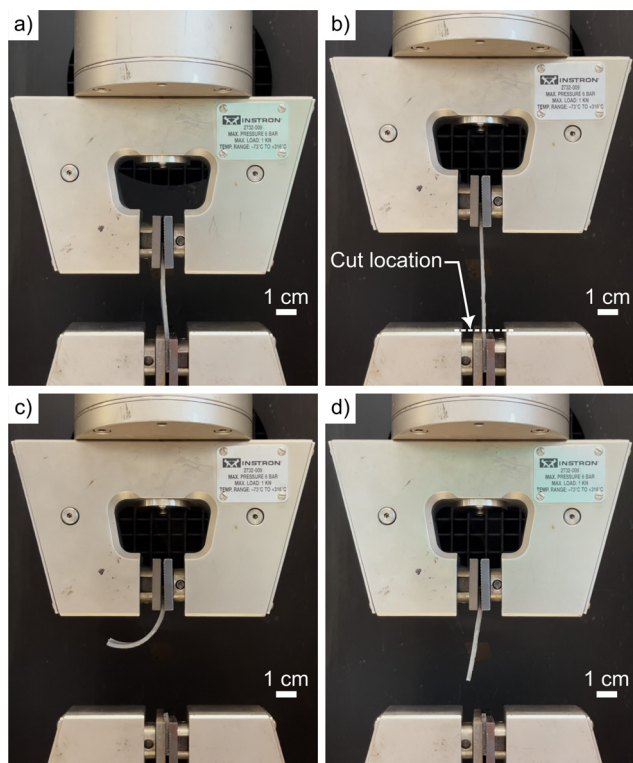
Fig. 1 Bilayer curvature testing procedure shown on a 20 mm extension test at a 2 mm s^{-1} extension rate with a hold time of 20 s. (a) The bilayer sample is pre-tensioned until taut before undergoing a constant rate extension. (b) The beginning of the bilayer sample's hold time following completion of extension. (c) The sample shown 1.20 seconds after cutting. (d) The sample after 10 minutes of relaxation.

Table 1 Bilayer curvature testing parameter overview

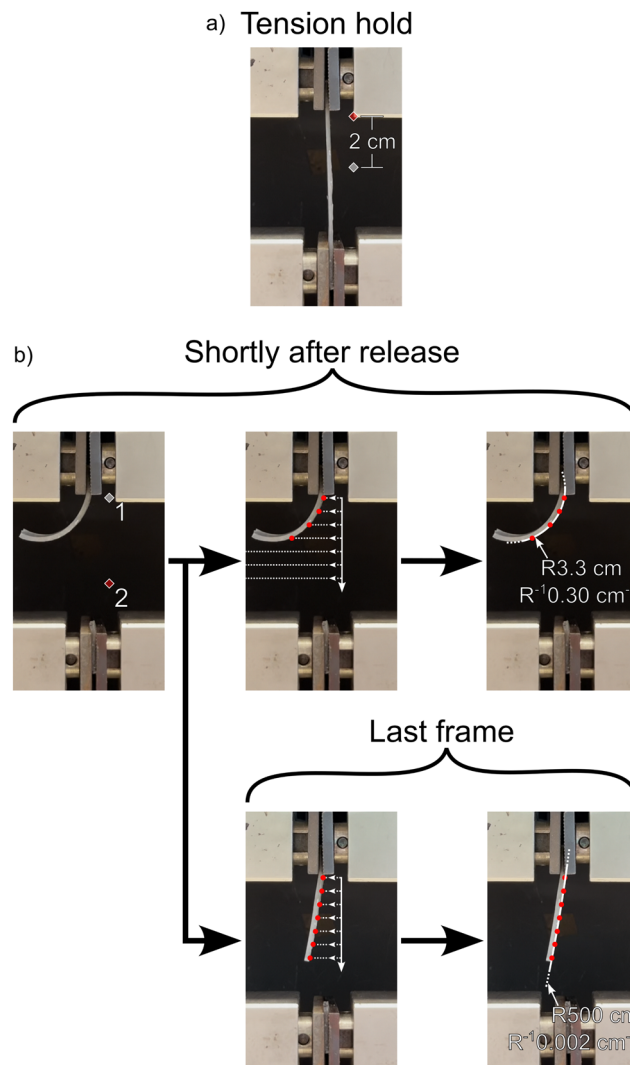| Extension (mm)	Extension rate (mm s^{-1})	Time held (s)
15	1	5
15	2	5
15	3	5
20	2	5
20	2	20
20	2	60
25	2	5
30	2	5

Fig. 2 Overview of MATLAB curvature tracking script process. (a) Pixel distance to real world distance calibration using user-defined clamp extension. (b) Two user-defined pixels form a vertical line. Scanning occurs to the left of the line until either a sufficiently grey pixel (shown as a red dot) is found and recorded or a timeout condition occurs, repeating the process for each vertical line pixel until the bottom of the line is reached. Circles (shown in white) are best fitted to the recorded points.

reacquired focus after cutting is displayed and a straight vertical line spanning the anticipated relaxed length of the strip is drawn using mouse input that is slightly offset from the rightmost side of the strip (Fig. 2b first panel). Each video frame is then sequentially analyzed during which each video pixel along the vertical line is inspected, starting from the vertical line and moving horizontally towards the left; if the video pixel has red, green, and blue decimal codes of each over 100, the pixel is grey, and assumed to be located on the right most side of the bilayer, and the location of the pixel is recorded (shown as red dots in Fig. 2b second and third panel). If no sufficiently grey pixel is found after scanning 300 pixels, a timeout condition occurs and no pixel is recorded for that

horizontal scan before attempting the next horizontal scan on the line below.

Following the last frame being analyzed, the rightmost pixels of the bilayer, corresponding to the outer radius, have been identified for each video frame. The pixels are then converted to positions in millimeters and best fit to a circle. Inverting the radii of the circles of best fit provides the curvatures over time. Certain bilayer strip tests exhibited high curvatures briefly following release; any left portion of the bilayer strips in this case that curves upwards enough to overlap horizontally with the right portion of the bilayer strip did not have the pixel defined curvatures of the left portion tracked by the script. This was deemed to not be a significant issue due to the apparent constant curvature bending radii early in the

bilayer's decaying curvature response. The script seemed to capture the curvature response accurately given the resolution limitations of the videos, apparent noise or oscillations in the curvature data is anticipated to be primarily caused by the top Instron grip fixture oscillating slightly due to the stress release from the cutting motion.

2.5 Bilayer adhesion testing

The adhesive strength of the SEPS-butyl and SIBS-butyl bilayers were evaluated using a T-peel test performed at room temperature using an Instron 5965 tensile tester (Instron Calibration Laboratory, MA, USA) equipped with a Cat. No. 2580-1KN load cell. For repeatable curling strong adhesion between layers is needed to transfer the stress across the bilayer interface. Five rectangular strips of ∼100 mm length and ∼13 mm width were hand cut from the prepared trilayer sheets. The open end of the trilayer sample, created from the foil, provided the tabs for the instron grips. A constant tensile extension rate of 50 mm min^{-1} was applied until the samples were fully delaminated or the maximum extension of the instrument (250 mm) was reached.

2.6 Intelligent structure and patterning

More complex bilayer architectures consisting of a cross and a two-segment alternating bilayer strip design were developed to investigate how well bilayer systems can be scaled up and implemented using alternative fabrication techniques and if the same principles of viscoelastic behavior apply.

A two-segment alternating bilayer strip design, shown in Fig. 3a, was chosen to investigate the behavior in which the distribution of viscoelastic properties varies along the length of a bilayer system. In order to maintain structural integrity, the SEPS component must be continuous across the length of a bilayer strip. However, butyl can alternate between different sides of the SEPS to influence the curvature.

A bilayer with a cross geometry design was also developed (Fig. 3b), with similar structures being commonly used in soft
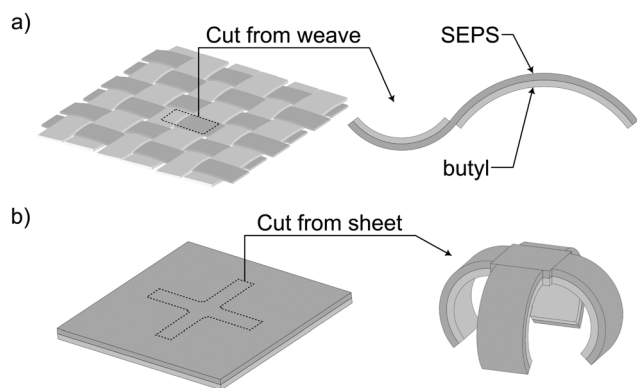

Fig. 3 Schematics showing a cut out from (a) an interwoven mesh of butyl and SEPS that forms the two-segment alternating bilayer strip and (b) a bilayer sheet that forms the bilayer cross, curling into a grasper following tensioning and release. Butyl is shown in light grey and SEPS is shown in darker grey.
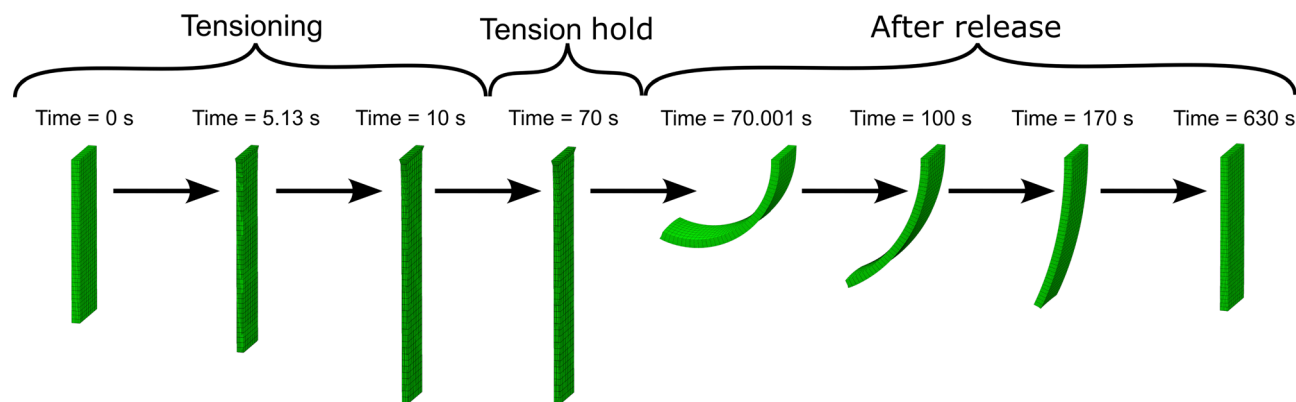
grippers for robotics. A template would be 3D printed with PLA filament and used to cut the desired shape with an X-Acto® knife.

2.7 FEA simulations of bilayer strips

FEA simulations of bilayer strip curvatures over time were performed using Abaqus/CAE 2022 FEA software to evaluate the performance of the material models compared to measured experimental curvature data scenarios (Fig. 4). The simulations are each composed of multiple Visco analysis steps with non-linear geometry enabled. Visco steps were used instead of dynamic steps because the overall curvature response of interest to this work was past the initial moments of curvature where inertial effects could have an appreciable influence. Within Fig. 4 the bilayer is shown to achieve maximum curvature after release within 1 ms, this is likely faster than reality and due to the lack of inertial effects considered in the simulation. The bilayers were modeled as a rectangular prism Abaqus part and the SEPS and butyl layers were geometrically partitioned and defined with Abaqus section assignments. The bilayers were modeled as having 36 mm length, matching the targeted curvature testing gauge length, and 12.7 mm width, matching the width of the die cut bilayers. The bilayer thickness in simulation varied depending on measured bilayer thicknesses from each curvature testing scenario, consisting of a certain extension, extension rate, and hold time. An averaged measured thickness of the SEPS and butyl over each repeated scenario (Table S2, ESI†) was implemented for each simulated scenario. Depending on the bilayer strip thickness, 2880–3520 elements with 3690–4428 nodes were used in the mesh. The mesh elements used were 8-node fully integrated linear bricks, hybrid, with constant pressure (C3D8H). Elements with hybrid formulation were used to prevent volumetric locking that commonly occurs in finite element simulations of materials that are nearly incompressible. Shear locking is mitigated through the use of 9 elements through the bilayer thickness (3 for the butyl, and 6 for the SEPS). A comparative study between linear and quadratic brick elements was performed on the highest strain energy scenario using the Generalized Maxwell model to ensure that significant differences in predicted curvature results were not present (Fig. S7, ESI†).

A viscoelastic strain error tolerance of 0.01 was used during all analysis steps. During simulations the linear elastic SEPS model was used in conjunction with the Maxwell and Zener viscoelastic butyl models, while the hyperelastic SEPS model was used in conjunction with the remaining models. The Maxwell and Zener models were paired with the linear elastic SEPS model to complement their simplicity. The parameters of all material models as implemented into Abaqus are provided in ESI,† Tables S3–S14.

The Abaqus analysis initial step begins with the bilayer strip in a flat state without stress. To recreate the experimentally measured bilayer response, the bilayer strip is aligned vertically and held fixed on the top faces using encastre boundary conditions.

The initial step is followed by a tensioning step during which a ramping displacement boundary condition is applied

Fig. 4 FEA bilayer strip simulation overview. The PRF power law 20 mm 2 mm s^{-1} 60 s simulation is shown.

that pulls the bilayer faces opposite the end of the fixed face for a distance and time corresponding to the simulated scenerio (Table S2, ESI†). A whole model standard (9.81 m s^{-2}) gravitational field is created, aligned axially downwards from the fixed faces. All extensions implemented in the simulations were reduced by 0.975 mm to attempt to account for the small portion of the bilayer strip remaining above the bottom grip surface of the tensile tester following the cutting of the samples with scissors.

Next, a step holding the bilayer stretched in place and propagating the boundary conditions and gravitational field occurs.

Following the hold step, a 1×10^{-6} s step during which the bilayer is retracted back to its original length using a ramping displacement boundary condition. This step was included to aid in convergence and decrease computational time. Varying material model simulations were run with and without this step and no appreciable effect was noticed on the curvature response. No automatic stabilization is used for this step as well as the tensioning and holding steps.

Next, a 560 s release step occurs during which the displacement boundary condition is deactivated and the bilayer is freely allowed to initially curve before relaxing back to the initial flat state over time. The release step uses automatic stabilization with a dissipated energy fraction of 0.0001 and an adaptive stabilization with a maximum ratio of stabilization to strain energy of 0.005. Varying amounts of stabilization were tested to ensure that the solution converged with decreasing amounts of stabilization (Fig. S8, ESI†). Noticeably, a larger stabilization value appears to increase the amount of time needed for the sample to reach maximum curvature following the release of tension. Stress, strain, and displacement were field output for the whole analysis.

3 Results and discussion

SEPS and butyl were modeled using various elastic and viscoelastic models (Fig. 5), respectively, and the models were implemented in Abaqus FEA for predicting curvatures. Relevant
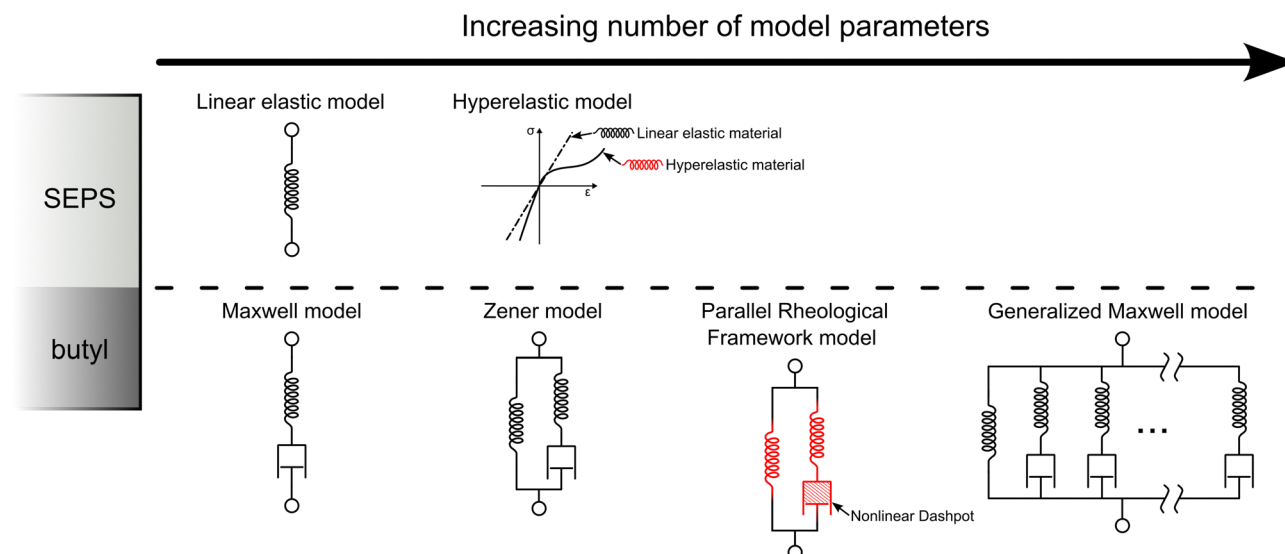

Fig. 5 Bilayer model overview. SEPS and butyl models shown in order of increasing number of model parameters.

mechanical testing data for both the elastic SEPS (Section 2.2) and viscoelastic butyl (Section 2.3) along with the interface (Section 2.5) was gathered from the Instron 5965 tensile tester. The mechanical testing was designed to target a "general-purpose" material response instead of testing only applicable to the specific curvature testing that was used to evaluate the models' performance. This was done so that the models would be versatile for use in a variety of simulated scenarios beyond the bilayer strip curvature simulations. The mechanical testing data was imported into MCalibration version 6.7.1 (Polymer-FEM LLC) where the optimization of model parameters for all models was performed. MCalibration simulates the entire strain history as used in our experiments, allowing the loading and unloading segments to be utilized for model fitting in addition to the relaxation segments.

3.1 SEPS elastic and hyperelastic modeling

To model the predominantly elastic SEPS material, linear elastic and hyperelastic models were optimized to fit experimental tensile data. Due to the anticipated engineering strains from curvature testing, the tensile data used for fitting the linear elastic model was between 0 and 1 engineering strain. For the hyperelastic model the engineering strain range used was between 0 and 7. Both the linear elastic and hyperelastic model were optimized to fit the 3rd tensile testing result, corresponding to the green line in Fig. S2 (ESI†). Tables S4 and S5 (ESI†) list the resulting optimized model parameters for the linear elastic and hyperelastic models, respectively. A nearly incompressible Poisson's ratio of 0.475 is assumed for the linear elastic model, in order to match the Abaqus hyperelastic default compressibility that was used. A Yeoh hyperelastic model was used due to a comparatively better fit to the tensile data when compared to other attempted I_1-based strain invariant hyperelastic models, Arruda–Boyce and neo-Hookean. The Yeoh hyperelastic model, building upon Ronald Rivlin's phenomenological theory of rubber elasticity,[37] incorporates a shear modulus that varies with deformation by the implementation of a strain energy function, U, which is cubic in I_1.[38] For this work, a compressible form of the Yeoh model based off Abaqus documentation[39] was used:

$$U = \sum_{i=1}^{3} C_{i0}\left(J^{-2/3}I_1 - 3\right)^i + \frac{1}{D_1}(J-1)^2 \tag{1}$$

where C_{i0} are fitted material constants, $J = \sqrt{I_3}$, I_1 and I_3 are strain invariants, and $D_1 = 2/k_0$ where k_0 is the initial bulk modulus. The optimized linear elastic and hyperelastic models fit their corresponding tensile data with normalized mean absolute difference (NMAD) fitness of 3.707 and 4.838, respectively. The NMAD fitness is defined as follows:

$$\text{NMAD} = 100 \times \frac{|\langle \mathbf{Y} - \mathbf{F} \rangle|}{\max(|\langle \mathbf{Y} \rangle|, |\langle \mathbf{F} \rangle|)} \tag{2}$$

where $\mathbf{Y}$ is a vector of the experimental stress data, $\mathbf{F}$ is a vector of the model predicted stress data, $\langle \square \rangle$ is the mean of the provided vector, and $|\square|$ is the absolute value of the provided

vector component. The NMAD fitness metric was chosen due to more significance being placed on larger magnitude absolute errors and is normalized for a more apt comparison between models.

3.2 Butyl viscoelastic modeling

The viscoelasticity of a polymeric material can be modeled as varying arrangements of springs and dashpots. Several viscoelastic models of increasing complexity were used to demonstrate their predictive capabilities of the butyl's viscoelastic response. While more complex and computationally expensive models might capture the butyl response more accurately, simpler models could suffice in certain circumstances such as those where computational speed is a priority. Within the viscoelastic models used within this work spring elements are chosen to be either a linear elastic or a nonlinear hyperelastic form; while dashpots are either linearly or nonlinearly dependent on $\dot{\varepsilon}$. Maxwell, Zener, Generalized Maxwell, and a 2 Network PRF model using Yeoh hyperelastic springs with a power law viscous flow dashpot were used as the focus of this work. Additionally, a modified hyperelastic Generalized Maxwell model and a two-network PRF model using Bergström–Boyce viscous flow were explored. The range of models in this work were chosen to show how varying model complexities would differ in their predictive capabilities of our bilayer systems, while certain models could perform worse they could also be computationally simpler which can be advantageous or practical in certain situations. Though the butyl exhibited an apparent Mullin's effect (Fig. S5, ESI†), the Mullins effect was not directly modeled to limit model complexity; though the Mullins effect is indirectly accounted for since the cyclic tension data used for model fitting would have been influenced by this Mullins effect. All of the butyl viscoelastic models were optimized to fit all three of the cyclic uniaxial tensile experiments (Fig. S4, ESI†) simultaneously.

The Maxwell model is the simplest representation of viscoelasticity, containing a linear elastic spring and a linear dashpot in series. It predicts a single relaxation time as a ratio of its two parameters: the dashpot's viscosity over the spring's stiffness. The optimized material parameters were a spring stiffness of 399.92 Pa and a viscosity of 21602.68 Pa s, corresponding to a relaxation time constant of 54.02 s (Table S7, ESI†). The optimized Maxwell model fit the experimental uniaxial tension data with an average NMAD fitness of 35.103.

The Zener model is composed of a Maxwell model (referred to as a Maxwell arm) with an additional linear elastic spring in parallel. While the singular relaxation time is still governed by the internal components of the Maxwell arm, the addition of the spring in parallel allows the model to have a driving force that over time returns the dashpot to its original length following a period of creep. The relaxation time constant of the optimized Zener model is 31.37 s (Table S8, ESI†). The optimized Zener model fit the experimental uniaxial tension data with an average NMAD fitness of 30.431.

The Generalized Maxwell model is a continuation of the Zener model with any desired number of additional Maxwell

arms. Unlike the Maxwell and Zener models which each have only a single relaxation time, the Generalized Maxwell model has a relaxation time associated with each additional Maxwell arm added, resulting in a superposition of all the relaxation times. Further, these relaxation times can be tuned for their strength or dominance in the overall response. For fitting the butyl uniaxial cyclic tension data, it was found that an optimized Generalized Maxwell model with seven Maxwell arms had an apparent converging minimization of error and as such seven Maxwell arms were used for the model within this work. The Maxwell arms of the model were implemented as a Prony series with relaxation time constants starting at 0.001 s and increasing by a single order of magnitude until reaching 1000 s (Table S8, ESI†). The most dominant relaxation times were 100 s, followed by 10 s, followed by 1000 s. The optimized Generalized Maxwell model fit the experimental uniaxial tension data with an average NMAD fitness of 24.845.

In addition to the standard Generalized Maxwell Model, a modified hyperelastic version was implemented. The hyperelastic modification involves replacing the single linear elastic spring arm with a Yeoh hyperelastic spring arm (Table S11, ESI†). The viscoelastic Prony series used in the standard Generalized Maxwell Model were also used in the modified version (Table S12, ESI†). The modified hyperelastic Generalized Maxwell Model fit the experimental uniaxial tension data with an average NMAD fitness of 17.821.

The PRF models, though similar schematically to the Zener model, differs by use of nonlinear springs and nonlinear dashpot elements. The PRF is a model framework used in Abaqus FEA to model nonlinear viscoelasticity, plasticity, and Mullins effect.[32] Specifically, the PRF model of focus in this work consists of a two-network model: the first network is composed of a singular Yeoh hyperelastic spring element which is in parallel with the second network, a Yeoh hyperelastic spring element in series with a nonlinear dashpot governed by the Power Law model. The Yeoh hyperelastic coefficients of the first network's element are defined and the stiffness of the second network's Yeoh spring element is defined using a ratio of the stiffness of the first element. The various dashpot behaviors commonly used in PRF models differ by their definition of an equivalent creep $\dot{\varepsilon}$ which is used to calculate the symmetric part of the velocity gradient as described in Abaqus documentation[39] as follows:

$$\mathbf{D}^{\mathrm{cr}} = \frac{3}{2\tilde{q}} \dot{\bar{\varepsilon}}^{\mathrm{cr}} \bar{\sigma} \tag{3}$$

where $\mathbf{D}^{\mathrm{cr}}$ is the symmetric part of the velocity gradient, $\tilde{q}$ is the equivalent deviatoric Cauchy stress, $\dot{\bar{\varepsilon}}^{\mathrm{cr}}$ is the equivalent creep strain rate, and $\bar{\sigma}$ is the deviatoric Cauchy stress. The Power Law model for the viscous dashpot behavior defines $\dot{\bar{\varepsilon}}^{\mathrm{cr}}$ as:

$$\dot{\bar{\varepsilon}}^{\mathrm{cr}} = \dot{\varepsilon}_0 \left\{ \left[\frac{\tilde{q}}{q_0 + a\langle p \rangle} \right]^n \left[(m+1)\bar{\varepsilon}^{\mathrm{cr}} \right]^m \right\}^{\frac{1}{m+1}} \tag{4}$$

where $\bar{\varepsilon}^{\mathrm{cr}}$ is the equivalent creep strain, $\tilde{q}$ is the equivalent creep strain, p is the Kirchoff pressure, and q_0, a, n, m, and $\dot{\varepsilon}_0$ are fitted

material parameters. The optimized Power Law PRF model fit the experimental unixial tension data with an average NMAD fitness of 16.414.

An additional similar PRF model that replaced the previous Power Law governed viscous flow with Bergström–Boyce flow was evaluated for comparison. The resulting model is similar to the viscoelastic Bergström–Boyce model, though Yeoh hyperelastic spring elements are utilized instead of the Arruda–Boyce hyperelastic elements found in the original Bergström–Boyce model.[40] The Bergström–Boyce flow defines $\dot{\bar{\varepsilon}}^{\mathrm{cr}}$ as follows:[39]

$$\dot{\bar{\varepsilon}}^{\mathrm{cr}} = \dot{\varepsilon}_0 (\lambda^{\mathrm{cr}} - 1 + E)^C \left(\frac{\tilde{q}}{q_0} \right)^m \tag{5}$$

where $\lambda^{\mathrm{cr}} = \sqrt{\frac{1}{3} \mathbf{I} : \mathbf{C}^{\mathrm{cr}}}$ and $\dot{\varepsilon}_0$, E, q_0, C, and m are fitted material parameters. The optimized Bergström–Boyce PRF model fit the experimental unixial tension data with an average NMAD fitness of 12.873.

3.3 Bilayer adhesion

In order to model a bilayer system, the interface between the two materials also needs to be explored. From the bilayer adhesion testing described in Section 2.5 the SEPS-butyl trilayer samples showed a high steady state force per unit width of $\sim$1900 N m^{-1} (Fig. 6). The observed dips were due to the presence of small air pockets at an interface of the butyl and SEPS. Care was taken to layer the films minimizing this trapped air, however complete air removal was unachievable due to the tackiness of the films. These artificial dips in stress had no lasting impact as the crack propagated around them returning to the steady state force. The fracture surfaces showed (Fig. S1, ESI†) high energy dissipation in the form of large fibrillation as the butyl layer underwent large engineering strains during the crack propagation. This cohesive failure is an indication of strong adhesion at the interface.[41]

In addition, SIBS-butyl trilayer samples as described in Section 2.5 were tested. SIBS was specifically identified for its high potential compatibility with butyl due to the identical nature of its middle block structure to that of the butyl.[42] A similarly high force per unit width of $\sim$1600 N m^{-1} (Fig. S6, ESI†) was observed
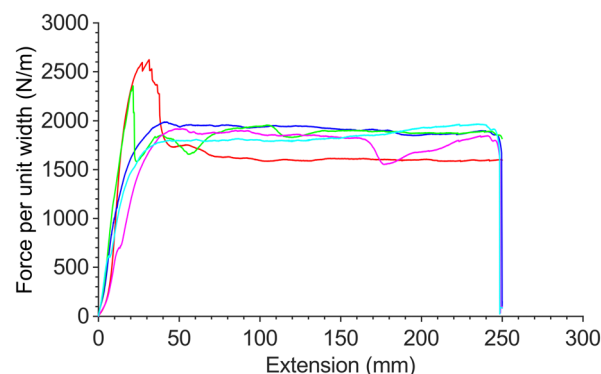

Fig. 6 SEPS-butyl adhesive testing results. Each coloured line corresponds to a different sample trial adhesive test.

along with cohesive failure. Interestingly the SIBS being a more elastic material stretched further during the peel testing resulting in a shorter overall crack propagation and more deformation to the butyl. This manifested itself in a longer time to reach steady state (~140 mm) as compared to SEPS (~50 mm). This may account for the slight dip in force per unit width as compared to SEPS. There were also less air pockets with the SIBS as its lower stiffness allowed for the air to escape during fabrication of the multi layer samples. Overall both materials exhibit strong adhesion and the interface can be assumed fixed for modeling purposes.

3.4 Predicted bilayer strip curvatures and time constants

The simulated bilayer strip curvatures were evaluated against the measured bilayer strip curvatures described in Section 2.4. The predicted curvatures from the four models of focus in this work are shown in Fig. 7 compared to their respective measured bilayer strip curvatures for each testing scenario. All of the measured data presented is shifted vertically such that the last data point has a curvature of 0 cm^{-1}. This shifting was done to counteract a curvature effect that the tensile tester grips had on the bilayer specimens where the samples would relax over time to a slightly curved state
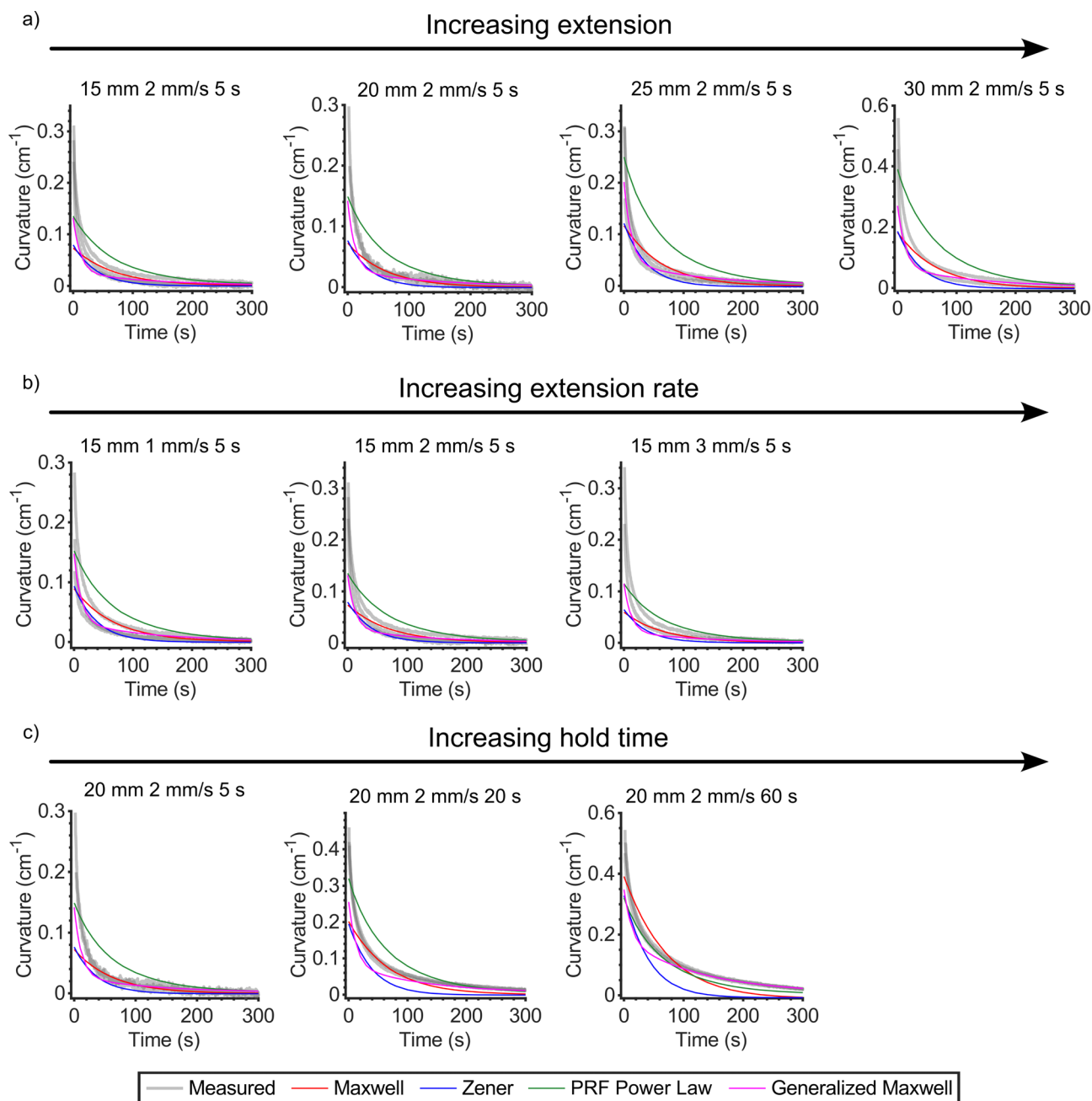

Fig. 7 Shifted measured curvatures and model predicted curvatures at varying extensions (a), extension rates (b), and hold times (c). Unshifted measured curvatures at a full-time span of 600 s are shown in ESI† (Fig. S9).

instead of returning to a fully vertical flat orientation. Upon removal of the samples from the grips the samples would relax over time to an expected flat orientation. This effect appeared to be caused by the portion of the relatively soft butyl layer being gripped being permanently deformed and spread out due to the grip force even though a relatively low grip pressure of $\sim$40 psi was used for this reason. A three-way analysis of variance (ANOVA) test was performed and showed that hold time but not extension and extension rate had a likely effect on the amount of residual curvature caused by the tensile tester grips (Tables S15 and S16, ESI†), with longer hold times corresponding with larger residual curvatures (p = 0.0103). This was further explored with another ANOVA test evaluating the total combined time under grip pressure during the tensioning and hold steps (Table S17, ESI†). Interestingly this showed a potential significance (p = 0.0889) but not to the same value as hold time alone.

The mean absolute scaled error (MASE)[43] in the form of mean absolute error divided by mean absolute deviation was chosen to assess the performance of the models against the experimental curvature data.

$$\text{MASE} = \frac{\langle|\mathbf{Y} - \mathbf{F}|\rangle}{\langle|\mathbf{Y} - \langle\mathbf{Y}\rangle|\rangle} \quad (6)$$

The averaged MASE fitness values for all models in varying curvature testing scenarios can be found in the ESI,† Table S1. When the MASE values from all the curvature testing scenarios are further averaged, it is shown that the Generalized Maxwell model has the lowest MASE of 0.360, followed by the Hyperelastic Generalized Maxwell's 0.378, and Maxwell's of 0.390. The Power Law and Bergström–Boyce flow PRF models had the largest averaged MASE values of 0.811 and 0.692, respectively. Further, the performance of the models was evaluated as a function of the number of parameters in each model (Fig. 9). While the Generalized Maxwell models had the lowest averaged MASE, they also had the highest number of model parameters, which could be a disadvantage in certain computational scenarios such as real-time simulation. Interestingly, the hyperelastic Generalized Maxwell model exhibits a slighter higher MASE value than the elastic Generalized Maxwell model. This discrepancy could potentially be attributed to the selection of the MASE fitness metric. For instance when the model predicted curvatures are evaluated using the NMAD fitness metric instead, the elastic Generalized Maxwell and hyperelastic Generalized Maxwell models have averaged NMAD fitness values of 35.009 and 33.931, respectively. The MASE fitness metric was chosen for use in this work due to its normalization and scaling of error, but like most fitness metrics it is not without its disadvantages, and as implemented in this work the MASE fitness metric will overly inflate error values as the experimental stress data approaches the mean of the experimental stress data. This possibility for artificial error inflation could potentially explain these slight unexpected numeric differences in the MASE fitness value results for the Generalized Maxwell models. The Maxwell model offers a similar averaged MASE to the Generalized Maxwell models while having the least amount of model

parameters. The model parameter count for each model includes their corresponding linear elastic or hyperelastic SEPS model parameters. The Poisson's ratio, D1, and the mass densities were not counted as model parameters.

Though several models appear to capture the majority of the curvature response over time, they all noticeably do not capture the maximum measured initial curvatures. We hypothesize that this is due to a combination of the chosen cyclic testing regime used for model fitting as well as a lack of inclusion of inertial effects in the simulations. The cyclic testing performed emphasizes slower strain rate events than what would occur specifically at the moment of sudden unloading with high strain energies that occurs when the bilayers are cut following tensioning. When looking at results from the test with the longest hold time, 60 s, our modeling appears to best capture this maximum curvature point when compared to the other testing scenarios. This is likely because the 60 s hold test has the least amount of strain energy upon release, which results in a slower strain rate as the bilayer goes to deflect upon being cut. To this end of high strain energies affecting the initial few seconds where maximum curvature is achieved, inertial effects could play a role in helping propel the bilayers to the higher maximum curvatures measured in reality. However, as stated in Section 2.7 the majority of the curvature response was the focus of this work which is why non-dynamic simulation steps were deemed suitable.

The relaxation time constants calculated from the shifted curvature data are presented in Fig. 8. Relaxation time constants are common ways to characterize how quickly a material changes, for example when a polymer is loaded to a certain strain value and then unloaded before reaching an equilibrium state. Specifically, defined as the time it takes for an initial value to decay to $1/e$ (36.8%) of that value.[44] We then took this definition of relaxation time constants and applied it to the curvature plots for our bilayers as shown in Fig. 7 and Fig. S10 (ESI†). While singular relaxation time constants are useful values for characterizing how fast a polymer system relaxes; they do not offer a complete characterization of the viscoelastic response on their own. For the plots presented in Fig. 8, instead of just evaluating this time constant at the initial point we repeatedly evaluated them throughout the time axis; such that points besides the initial maximum curvature point are selected and evaluated for how long of a time it takes them to get to $1/e$ of their present curvature value. This shows how a calculated relaxation time constant can be thought of as changing over time. These results show how the Generalized Maxwell model with multiple superimposed relaxation time constants, effectively varies over time to align with measured data. The Generalized Maxwell model shows the best overall initial matching of the measured relaxation time constants and is in general able to best match the beginning upwards trend that the measured data shows. The Power Law PRF model also consistently shows an upwards initial trend though with a noticeably more inaccurate fit compared to the Generalized Maxwell model. The Maxwell and Zener models often show a constant relaxation time constant as expected though start to
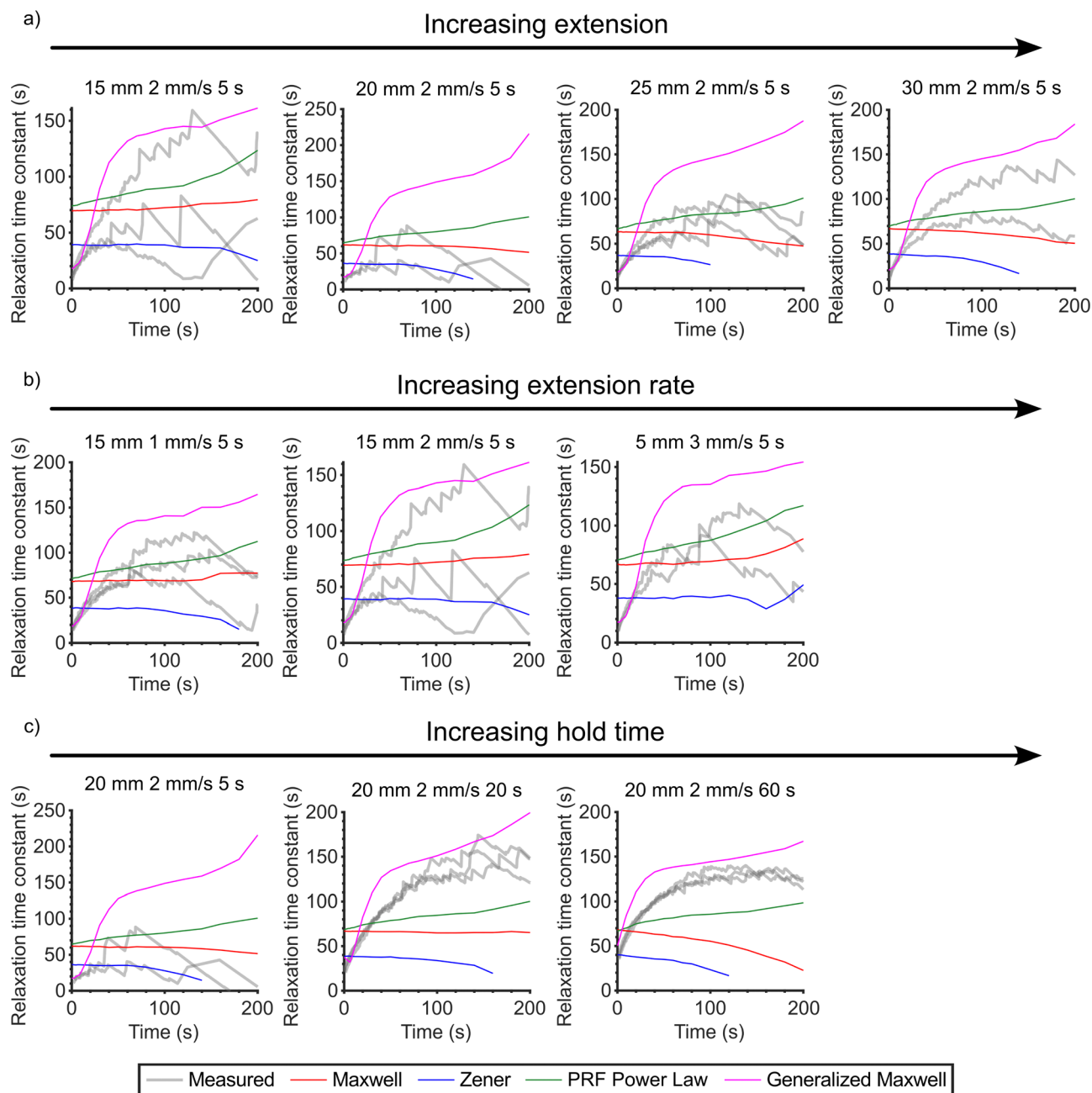
Fig. 8 Curvature relaxation time constant results for shifted measured data and models at varying extensions (a), extension rates (b), and hold times (c).

diverge towards the end of their data curves likely due to numerical sensitivities in the time constant calculations. The curvature and relaxation time constant results for the hyperelastic Generalized Maxwell and Bergström–Boyce flow PRF models are shown in the ESI,† Fig. S10 and S11, respectively.

3.5 Intelligent structures

The alternating bilayer strip and bilayer cross designs discussed in Section 2.6 were fabricated (Fig. 10). We hypothesized that the alternating bilayer strip would lead to multi-segment curvature, while still allowing for full recovery of the initial shape. In a two-segment alternating bilayer, following a tension

and release we clearly see this phenomenon (Fig. 10b). The idea of multi-segment curvatures could be further explored by the fabrication of alternating bilayer strips with more than two-segments as well as implementing them into interlocking architectures or as metamaterials. Further, bilayer segments with varying thicknesses along their lengths would lead to non-constant radii of curvatures, allowing more possibilities for future designs.

The bilayer cross design demonstrated that tension along any axis can produce the same characteristic bending and retraction seen in individual bilayer strips. Further, the bilayer cross is capable of grasping and releasing objects, such as a foam piece shown in Fig. 10d at a set time interval. Future
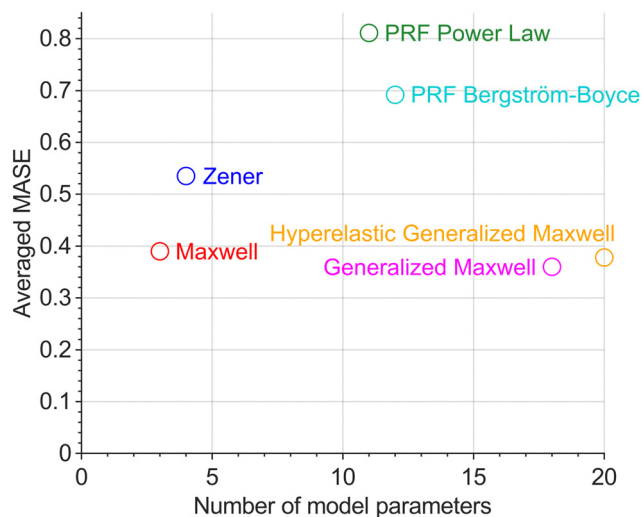
Fig. 9 Averaged MASE across all tests vs number of model parameters. Averaged MASE values per test are shown in ESI,† Table S1.
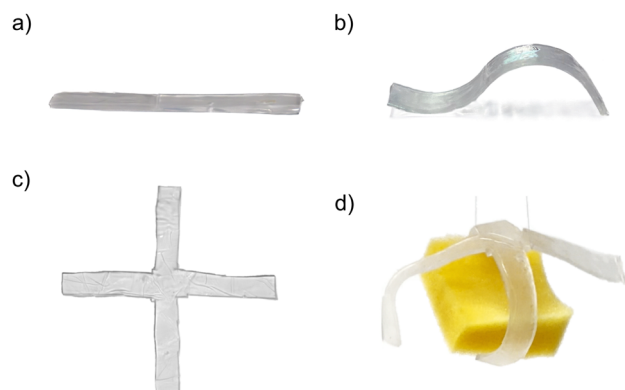

Fig. 10 Photographs of the two-segment alternating bilayer strip and bilayer cross. The two-segment alternative bilayer shown (a) fully relaxed and (b) shortly following tensioning and release. The bilayer cross shown (c) fully relaxed and (d) grasping a foam piece following tensioning and release (Movie S1, ESI†).

implementations of the grasper could involve a dedicated tensioning mechanism for the four arms in their flat resting position and upon tension release the arms would then grasp and passively release after a certain time without further intervention. This is in contrast to many existing grasper designs that require discrete actuating signals for both the grasping and the releasing motion. The soft arms could be designed to compliantly deform to a variety of objects or specialized to conform closely to certain awkward shapes. The passive release timings could be tuned by either the composition and shape of the arms or by controlling the tension initially applied.

4 Conclusions

Viscoelastic bilayer systems offer a unique opportunity to intelligently preprogram a response and our work demonstrates how to predict that response by building upon our understanding of polymer material properties and model-based simulations. In order to better characterize this bilayer response we fabricated several SEPS-butyl bilayer strips and analyzed their curvature response with varying viscoelastic loading parameters: extension, extension rate, and hold time. Model-based FEA simulations of the viscoelastic bilayer strips and varying loading parameters were compared to measured real-world curvatures. The Generalized Maxwell butyl models in conjunction with a Yeoh hyperelastic SEPS model had the lowest averaged MASE when compared to the measured curvatures over time. This is likely due to its superposition of multiple relaxation time constants. However, the Maxwell butyl model in conjunction with the linear elastic SEPS model offers a suitable alternative with only 8% higher MASE while being computationally simpler, which could be advantageous in certain scenarios such as real-time simulations.

Accurate simulations allow one to design for and predict the bilayer system response prior to fabrication, saving time and iterations in the design process. Additionally, the simulations could be run in real-time for the purpose of closed-loop control systems that make use of these shape-morphing polymer materials. To demonstrate more advanced bilayer architectures, a two-segment alternating bilayer strip design and a cross design capable of grasping and releasing objects were fabricated. The resulting motions for these designs are distinct from those of a simple bilayer strip, but ultimately, the same viscoelastic principles apply.

With the framework developed within this work, several future improvements can be pursued. Alternative bilayer materials such as SIBS, which has greater structural compatibility with butyl, could be further developed. Getting the bilayers to adhere to each other is not always trivial. Adhesion between layers can depend on many factors, such as bubbles forming while melt pressing the films, entanglements at the interface, and polymer synthetic limitations. The influence of these factors will be explored in greater depth in future work, as we expect bilayer performance to be closely linked to chemical and physical architecture at the interface. Additional characterization of the interface adhesion and bilayer response from varying molecular weights across both components and block ratios in the triblock elastomers could be performed. The viscoelastic material models could potentially be further improved by accounting for the stress softening Mullins effect, which could provide more accurate simulations in situations with repeated tensioning in a short period of time. The cyclic testing used for fitting the butyl models could be modified or further supplemented to explore the effects of longer relaxation holds and higher strain rates to potentially improve model accuracy. Dynamic simulation steps could be utilized to capture inertial effects, especially during the initial curvatures. The use of higher-order elements while also potentially reducing the overall number of elements could be examined. Varying time constants and the number of time constants in the Generalized Maxwell models could be explored to produce adequate models using fewer parameters. Intricate bilayer architectures could be

fabricated *via* alternative manufacturing routes such as 3D printing which offers a solution to fabricating both more complex overall structural geometries as well as varying bilayer material ratios at the interface. Further improvements of bilayer manufacturing and modeling capabilities could play an integral role in the development of bilayer systems for use in soft robotics where both intelligent soft body design and control are often challenges.

Author contributions

A. M., E. C., Z. B., and G. W. led the development of concepts. A. M. and E. C. designed the experiments. A. M., E. C., and Z. B. interpreted the results. Z. B. performed the individual film, bilayer, and trilayer fabrications. Z. B. and E. C. assembled cross and weave geometries from bilayer sheets. A. M. and E. C. established a proof of concept gripper from SEPS-butyl bilayer. Z. B. performed the mechanical testing on individual films and the trilayer adhesion testing. A. M., E. C., and Z. B. performed the curvature testing on bilayer strips. A. M. performed bilayer video curvature tracking, model-fitting, and FEA simulations. A. M. created the figures and tables. A. M. and Z. B. performed statistical analysis of the results. A. M., E. C., and Z. B. wrote the paper. G. W and K. D. assisted with paper revisions. G. W. and K. D. secured funding, initiated the proposal for modeling and testing of elastic/viscoelastic bilayer systems, and supervised the project.

Conflicts of interest

There are no conflicts to declare.

Acknowledgements

Notes and references

1 C. Fang, J. Leng, H. Sun and J. Gu, *Mech. Mater.*, 2018, **120**, 34–42.
2 S. Poppinga, C. Zollfrank, O. Prucker, J. Rühe, A. Menges, T. Cheng and T. Speck, *Adv. Mater.*, 2018, **30**, 1703653.
3 R. Diaz-Calleja, D. Ginestar, V. Compañ Moreno, P. Llovera-Segovia, C. Burgos-Simón, J. C. Cortés, A. Quijano and J. Díaz-Boils, *Polymers*, 2021, **13**, 2198.
4 Y. Dong, J. Wang, X. Guo, S. Yang, M. Ozen, P. Chen, W. Du, F. Xiao, U. Demirci and B.-F. Liu, *Nat. Commun.*, 2019, **10**, 1–10.
5 C. Dingler, H. Müller, M. Wieland, D. Fauser, H. Steeb and S. Ludwigs, *Adv. Mater.*, 2021, **33**, 2007982.
6 P. Prathumrat, M. Nikzad, E. Hajizadeh, R. Arablouei and I. Sbarski, *Polym. Adv. Technol.*, 2022, **33**, 1782–1808.
7 S. Mirvakili and I. Hunter, *Adv. Mater.*, 2017, **30**, 1704407.
8 S. Coyle, C. Majidi, P. Leduc and K. Hsia, *Extreme Mech. Lett.*, 2018, **22**, 51–59.
9 S. Kim, C. Laschi and B. Trimmer, *Trends Biotechnol.*, 2013, **31**, 287–294.
10 L. F. Muff and C. Weder, *Adv. Intell. Syst.*, 2023, **5**, 2200265.
11 B. J. Cafferty, V. E. Campbell, P. Rothemund, D. J. Preston, A. Ainla, N. Fulleringer, A. C. Diaz, A. E. Fuentes, D. Sameoto and J. A. Lewis, *et al.*, *Adv. Mater. Technol.*, 2019, **4**, 1800299.
12 J. Huang, J. Liu, B. Kroll, K. Bertoldi and D. R. Clarke, *Soft Matter*, 2012, **8**, 6291–6300.
13 C. E. Wisinger, L. A. Maynard and J. R. Barone, *Soft Matter*, 2019, **15**, 4541–4547.
14 S. Timoshenko, *J. Opt. Soc. Am.*, 1925, **11**, 233–255.
15 L. F. Muff, A. S. Mills, S. Riddle, V. Buclin, A. Roulin, H. J. Chiel, R. D. Quinn, C. Weder and K. A. Daltorio, *Adv. Mater.*, 2023, 2210409.
16 S. Bartels, A. Bonito, A. H. Muliana and R. H. Nochetto, *J. Comput. Phys.*, 2018, **354**, 512–528.
17 F. Greco, V. Domenici, A. Desii, E. Sinibaldi, B. Zupančič, B. Zalar, B. Mazzolai and V. Mattoli, *Soft Matter*, 2013, **9**, 11405–11416.
18 W. Wang, C. Xiang, Q. Zhu, W. Zhong, M. Li, K. Yan and D. Wang, *ACS Appl. Mater. Interfaces*, 2018, **10**, 27215–27223.
19 T. Wang, J. Zhao, C. Weng, T. Wang, Y. Liu, Z. Han and Z. Zhang, *Composites, Part A*, 2021, **144**, 106322.
20 Y. Hu, J. Liu, L. Chang, L. Yang, A. Xu, K. Qi, P. Lu, G. Wu, W. Chen and Y. Wu, *Adv. Funct. Mater.*, 2017, **27**, 1704388.
21 M. Ding, L. Jing, H. Yang, C. Machnicki, X. Fu, K. Li, I. Wong and P.-Y. Chen, *Mater. Today Adv.*, 2020, **8**, 100088.
22 M. Dai, O. T. Picot, J. M. Verjans, L. T. de Haan, A. P. Schenning, T. Peijs and C. W. Bastiaansen, *ACS Appl. Mater. Interfaces*, 2013, **5**, 4945–4950.
23 F. Héraly, M. Zhang, A. Åhl, W. Cao, L. Bergström and J. Yuan, *Adv. Intell. Syst.*, 2022, **4**, 2100084.
24 X. P. Hao, C. W. Zhang, W. Hong, M. Meng, L. X. Hou, M. Du, Q. Zheng and Z. L. Wu, *Mater. Horiz.*, 2023, **10**, 432–442.
25 J. G. Drobny, *5 - Styrenic Block Copolymers*, William Andrew Publishing, Oxford, 2nd edn, 2014, pp. 175–194.
26 G. Kaszas, J. Puskas and W. Baade, in *Polymeric Materials Encyclopedia*, ed. J. Salamon, CRC Press, Inc., 1996, pp. 175–177.
27 D. Barczikai, J. Domokos, D. Szabó, K. Molnar, D. Juriga, E. Krisch, K. S. Nagy, L. Kohidai, C. A. Helfer and A. Jedlovszky-Hajdu, *et al.*, *Molecules*, 2021, **26**, 5207.
28 Y. Dikici, H. Jiang, B. Li, K. A. Daltorio and O. Akkus, *Adv. Eng. Mater.*, 2022, **24**, 2101620.
29 J. Wong, A. Basu, M. Wende, N. Boechler and A. Nelson, *ACS Appl. Polym. Mater.*, 2020, **2**, 2504–2508.
30 R. Christensen, *Theory of viscoelasticity: an introduction*, Elsevier, 2012.
31 P. J. Carreau, D. C. De Kee and R. P. Chhabra, *Rheology of polymeric systems: principles and applications*, Carl Hanser Verlag GmbH Co KG, 2021.

32 J. Hurtado, I. Lapczyk and S. Govindarajan, *Const. Models Rubber*, 2013, **8**, 95–100.

33 K. Kunal, M. Paluch, C. M. Roland, J. E. Puskas, Y. Chen and A. P. Sokolov, *J. Polym. Sci., Part B: Polym. Phys.*, 2008, **46**, 1390–1399.

34 H. Pouriayevali, Y. Guo and V. Shim, *Int. J. Impact Eng.*, 2012, **47**, 71–78.

35 E. Sachyani Keneth, A. Kamyshny, M. Totaro, L. Beccai and S. Magdassi, *Adv. Mater.*, 2021, **33**, 2003387.

36 L. Mullins, *Rubber Chem. Technol.*, 1969, **42**, 339–362.

37 R. S. Rivlin, *Philos. Trans. R. Soc., A*, 1948, **241**, 379–397.

38 O. H. Yeoh, *Rubber Chem. Technol.*, 1993, **66**, 754–771.

39 *SIMULIA User Assistance 2022 Abaqus Documentation*, Dassault Systems Simulia Corporation, 2022, **https://help. 3ds.com/2022/English/DSSIMULIA_Established/SIMULIA_ Established_FrontmatterMap/sim-r-DSDocAbaqus.htm?cont- extscope=all**.

40 J. S. Bergström and M. Boyce, *J. Mech. Phys. Solids*, 1998, **46**, 931–954.

41 R. Villey, P.-P. Cortet, C. Creton and M. Ciccotti, *Int. J. Fract.*, 2017, **204**, 175–190.

42 G. Kaszas, J. Puskas, J. Kennedy and W. Hager, *J. Polym. Sci., Part A: Polym. Chem.*, 1991, **29**, 427–435.

43 R. J. Hyndman and G. Athanasopoulos, *Forecasting: principles and practice*, OTexts, 2018.

44 G. R. Strobl and G. R. Strobl, *The physics of polymers*, Springer, 1997, vol. 2.